nature communications

Article

https://doi.org/10.1038/s41467-024-54318-7

Parameterization and quantification of two key operando physio-chemical descriptors for water-assisted electro-catalytic organic oxidation

Received: 31 January 2024

Accepted: 4 November 2024

Published online: 22 November 2024

Check for updates

Bailin Tian[1,3], Fangyuan Wang[1,3], Pan Ran[1], Luhan Dai[1], Yang Lv[1], Yuxia Sun[1], Zhangyan Mu[1], Yamei Sun[1], Lingyu Tang[1], William A. Goddard III[2] & Mengning Ding[1]

Electro-selective-oxidation using water as a green oxygen source demonstrates promising potential towards efficient and sustainable chemical upgrading. However, surface micro-kinetics regarding co-adsorption and reaction between organic and oxygen intermediates remain unclear. Here we systematically study the electro-oxidation of aldehydes, alcohols, and amines on Co/Ni-oxyhydroxides with multiple characterizations. Utilizing Fourier transformed alternating current voltammetry (FTacV) measurements, we show the identification and quantification of two key *operando* parameters ($\Delta I_{harmonics}/I_{OER}$ and $\Delta V_{harmonics}$) that can be fundamentally linked to the altered surface coverage ($\Delta\theta_{OH^*}/\theta^{OER}_{OH^*}$) and the changes in adsorption energy of vital oxygenated intermediates ($\Delta G^{EOOR}_{OH^*} - \Delta G^{OER}_{OH^*}$), under the influence of organic adsorption/oxidation. Mechanistic analysis based on these descriptors reveals distinct optimal oxyhydroxide surface states for each organics, and elucidates the critical catalyst design principles: balancing organic and $M^{3+\delta}$–OH* coverages and fine-tuning ΔG for key elementary steps, e.g., via precise modulation of chemical compositions, crystallinity, defects, electronic structures, and/or surface bimolecular interactions.

Oxygen evolution reaction (OER) is an important electrochemical half-reaction in water electrolysis, but its slow kinetics has severely restricted the overall catalytic/energy efficiency for hydrogen production[1–4]. Recently, the electro-oxidation of biomass-derived molecules (such as aldehydes, alcohols, and amines) have been recognized as a more sustainable and efficient method[5–7] to replace OER in the overall water electrolysis, or to serve as a potential methodology for the green and safe production of value-added chemical stocks[8–15]. To this end, cobalt/nickel-based hydroxides and oxyhydroxides are widely used as low-cost OER electrocatalysts[16–29]. The oxygenated species adsorbed on high-valence transition metals are generally accepted as key intermediates during OER[30–37]. Due to their excellent OER activity, the Co/Ni-based compounds (of which the active species are typically oxyhydroxides under applied anodic potentials) have been employed for the electro-oxidation of biomass-derived molecules in most recent studies[38–44]. To meet the criteria of optimized *operando* surface coverage of key intermediate species[45], transition metal doping in Co/Ni oxyhydroxides usually leads to improved catalytic performance. For example, recent studies revealed that while Ir/Rh dopants significantly promote the oxygen radical

[1]Key Laboratory of Mesoscopic Chemistry, School of Chemistry and Chemical Engineering, Nanjing University, Nanjing, Jiangsu, China. [2]Materials and Process Simulation Center (MSC) and Liquid Sunlight Alliance (LiSA), California Institute of Technology, Pasadena, CA, USA. [3]These authors contributed equally: Bailin Tian, Fangyuan Wang. e-mail: mding@nju.edu.cn

formation[30,46] and thus the OER performance, Mn/Cu doping better balances the adsorptions of organic substrates and surface oxygen species on NiOOH, to achieve the highest conversion rates and Faradaic efficiencies (FEs) for selective oxidation of amines/alcohols[11,47–51].

The kinetic analysis for selective electro-oxidative conversion of different organic molecules is shown in Fig. 1a (also see Supplementary Figs. S1, S2), which suggest a general surface bimolecular reaction (Langmuir-Hinshelwood) mechanism for the R-CHO, R-CH_2OH, and R-CH_2NH_2 molecules. This is consistent to the proposed key surface process including both adsorbed organic molecules and surface oxygenated species from partial water oxidation. The corresponding surface reaction pathways are illustrated in Fig. 1b. These kinetic data further reveal electro-oxidation rate vertexes in regards to the concentrations (surface coverages) of the furfural and furfuryl alcohol molecules (solid curves in Fig. 1a, the kinetic data of other molecules can be found in Supplementary Fig. S2), which clearly indicates the importance of balancing these surface parameters for their optimal reaction efficiency[52]. The recently developed micro-kinetic simulation[45,53–55] provides a theoretical means to evaluate the surface coverages of different intermediates, and Fig. 1c demonstrates the simulation results of various intermediates following the EOOR pathways (Eqs. 1–9). However, as the key parameters used in simulation were typically estimated values (Table S1), the precise experimental quantification of these surface parameters regarding both organic[56] and active oxygenated intermediates[57] under comprehensive electrochemical *operando* conditions remain challenging. As a result, the lack of precise, *operando* surface kinetic details have restricted the rational catalyst design and methodology development for selective electro-oxidation of diverse chemical stocks.

Here we report the parameterization, experimental quantification and corresponding mechanistic investigations on the micro-electro-kinetic behaviors of a series of NiCo hydroxides (α-$Co_xNi_{1-x}(OH)_2$) with varying Ni/Co ratios for the electro-oxidation of different model organic molecules (aldehyde, alcohol, and amine). In situ electrical transport measurements (ETS)[58–60] revealed an insulator-semiconductor phase transition[30] that correlates to high-valence $Co^{3+\delta}$–OH*/O* formation in α-$Co(OH)_2$, and their consumptions during the oxidation of organic substances. Additional in situ spectroscopic results demonstrated that α-$Co_xNi_{1-x}(OH)_2$ with different Ni/Co ratios exhibited preferential activities towards either OER or EOOR. Furthermore, Fourier-transformed alternating current voltammetry (FTacV) measurements[61] were successfully conducted on the α-$Co_xNi_{1-x}(OH)_2$ under *operando* electro-oxidation conditions. From high-order FTacV harmonics we extract two key parameters, the $\Delta I_{harmonics}/I_{OER}$ and the $\Delta V_{harmonics}$, which correlate quantitatively to i) the relative change in surface coverage of $M^{3+\delta}$–OH* ($\Delta\theta_{OH^*}/\theta_{OH^*}^{OER}$) from OER to EOOR, and ii) altered Gibbs free energy change of the M^{IV}–OH* formation step ($\Delta\Delta G_{OH^*}^{EOOR-OER} = \Delta G_{OH^*}^{EOOR} - \Delta G_{OH^*}^{OER}$) under the influence of organic adsorption/oxidation, respectively. Catalytic activity diagrams

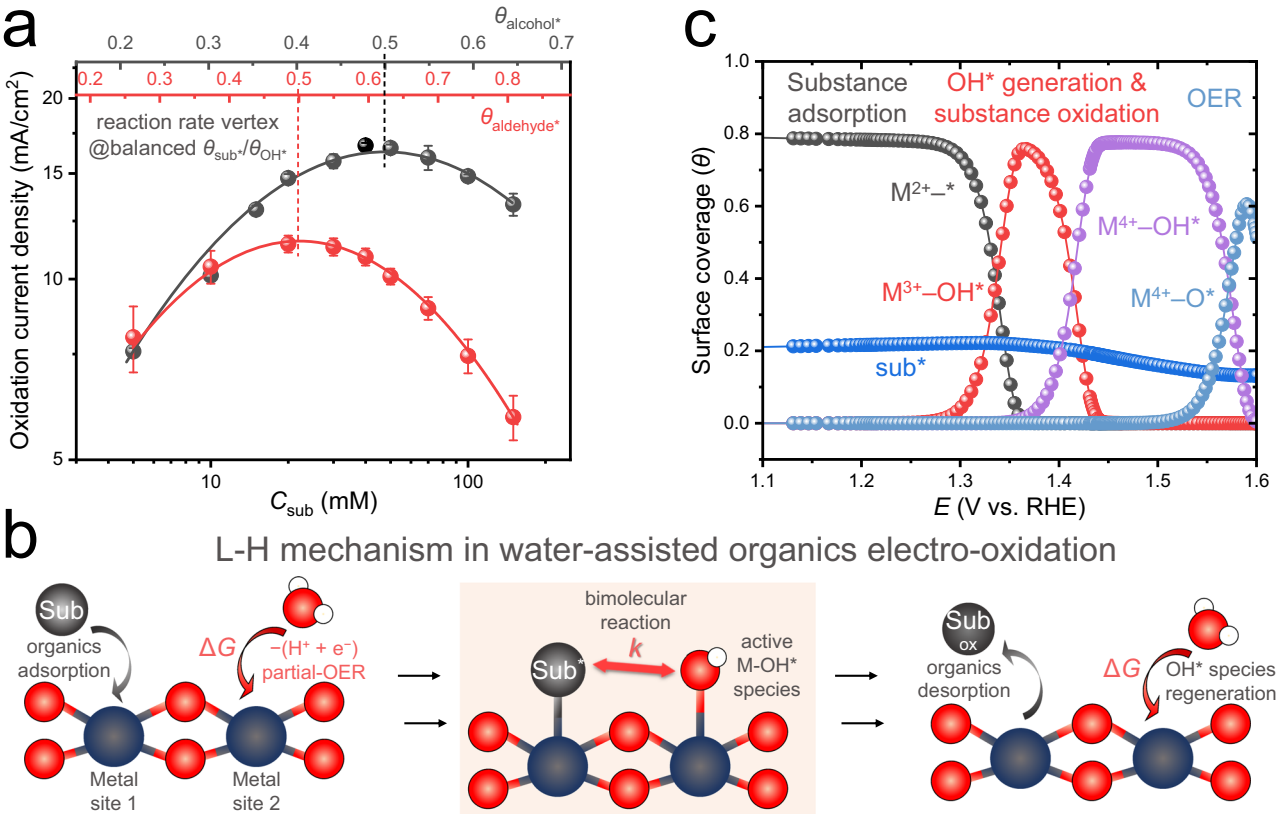

Fig. 1 | Reaction pathway and kinetics in the water-oxidation-assisted selective electro-oxidation reaction following a surface bimolecular reaction (Langmuir-Hinshelwood) mechanism. a Experimental and simulated reaction rates of organic electro-oxidation following the Langmuir-Hinshelwood (L-H) mechanism, using furfuryl alcohol (black) and furfural (red) as the example. Round points depict the experimental partial current densities (for organic oxidation) over the organic substrate concentrations (C_{sub}). Error bars were obtained from three independent experiments. Solid curves illustrate the simulated reaction rates as a function of θ_{sub*}, with a fixed bulk pH value (i.e., C_{OH^-} = 1 M, which would not change significantly during the whole reaction). **b** The schematic illustration of the surface co-adsorption of organic molecules and active OH* species and the bimolecular reaction (highlighted in shading) between them. The dark blue and red balls represent the metal site and oxygen atom, respectively. "Sub" represents the organic substance (R-CHO, R-CH_2OH, and R-CH_2NH_2 in this work), "Sub-ox" represents the oxidation product and superscript "*" indicates the adsorbed species. **c** The typical microkinetic simulation of the surface coverages of possible species for α-$Ni(OH)_2$.

constructed by these two physio-chemical descriptors show characteristic reactive regions that correspond to different organic oxidation behaviors on the Co/Ni oxyhydroxides. It can be concluded that different organic molecules (R-CHO, R-CH_2OH, and R-CH_2NH_2) possess varying thermodynamic oxidation potentials and reaction complexities (i.e., number of reaction steps and total consumption of oxygenated species), and therefore demonstrate different preferences on the θ_{OH^*} and the ΔG_{OH^*} parameters for their optimized electro-oxidation efficiencies. Overall, the $\Delta\theta_{OH^*}/\theta_{OH^*}^{OER}$ and $\Delta\Delta G_{OH^*}^{EOOR-OER}$ descriptors provide quantitative *operando* surface information that are key to the optimization of reaction performance (yield, FE, etc.) for specific target reactions, which lead to effective guidance for rational catalyst design and modulation.

Results and discussion

In situ qualitatively characterizations of the generation of active oxygenated species and their consumption under organic oxidation

Similar to Ni hydroxides in Fig. 2a[30], the in situ electrical transport spectroscopy (ETS) results of α-$Co(OH)_2$ (XRD pattern can be found in

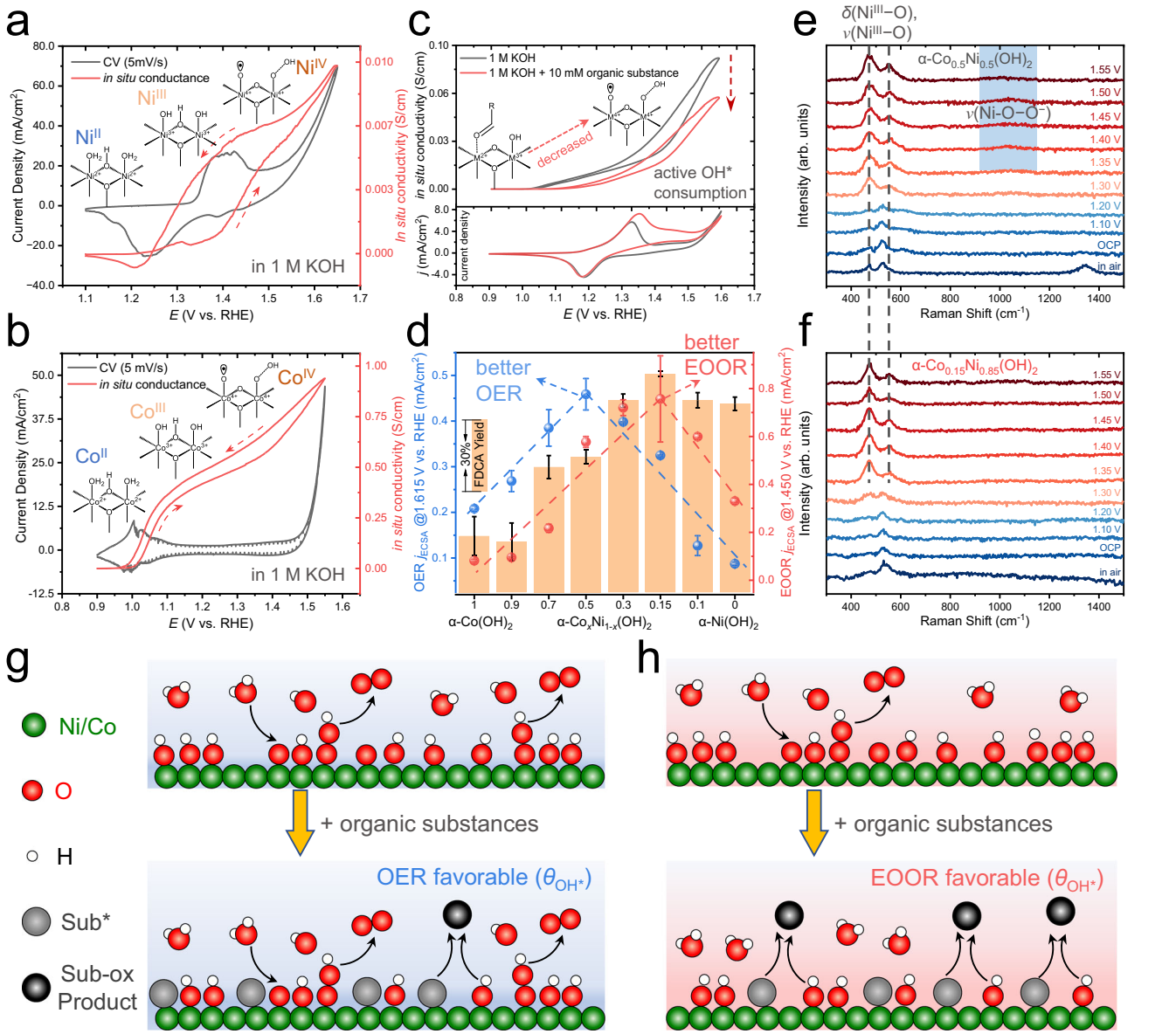

Fig. 2 | The in situ measurements of α-$Co_xNi_{1-x}(OH)_2$ reveal the active oxygenated species generation and their consumption by organics. On-chip CV and in situ electrical transport (ETS) signals of α-$Ni(OH)_2$ (**a**), α-$Co(OH)_2$ (**b**) in 1.0 M Fe-free KOH with a slow scan rate (5 mV/s) of electrochemical potential. The red dashed arrows indicate the potential scan direction. **c** The typical ETS signals obtained in 1.0 M KOH and with the addition of 10 mM organic substance (HMF, 5-hydroxymethylfurfural) for α-$Co_{0.5}Ni_{0.5}(OH)_2$ (upper part) and its CV curves in the condition of OER and EOOR (bottom part). The arrow indicates the decreased in situ conductivity due to OH* consumption. **d** The catalytic activities (normalized by roughness factor) of OER and EOOR of different α-$Co_xNi_{1-x}(OH)_2$ ($x = 0$–1), where two sets of volcano-like correlations (guided by dashed blue and red lines) can be observed. The yield of FDCA (2,5-furandicarboxylic acid) products (orange column) in bulk electrolysis is also presented. Error bars were obtained from three independent electro-organic oxidation reactions. All electrochemical data were presented without *iR*-correction. The size of carbon papers (C.P.) were 1 × 2 cm^2. The in situ Raman spectroscopy characterizations of α-$Co_{0.5}Ni_{0.5}(OH)_2$ (**e**) and α-$Co_{0.15}Ni_{0.85}(OH)_2$ (**f**) during EOOR, where the $\delta(Ni^{III}–O)$ (~480 cm^{-1}), $\nu(Ni^{III}–O)$ (~550 cm^{-1}) and O–O^- peak (~1060 cm^{-1}) are labeled in dashed lines and blue rectangles, respectively. **g**, **h** Schematic illustration of surface processes and the characteristic change in surface OH* coverage on the catalysts that favor OER and EOOR pathway, respectively. The green, red, white, gray, and black circles represent Ni/Co, O, H, adsorbed substance, and oxidized products, respectively.

Supplementary Fig. S6a) indicates a clear insulator-to-semiconductor phase transition accompanied by the oxidation of Co to a high-valent state and the corresponding evolution of oxygenated species (Fig. 2b, also see Supplementary Fig. S13). The in situ conductance of α-$Co(OH)_2$ can be partitioned into three regions:

i) At the initial stage, the Co^{II}–H_2O* in the hydroxide shows an insulating feature. When electrochemical potentials are scanned in the positive direction, the oxidation of Co^{II} and the formation of Co^{III}–OH* species (starting from 1.00–1.10 V_{RHE}) first leads to an inclining conductance, probably due to double-exchange interactions[30,62–64] between Co^{II}-O-Co^{III} (analogous to Ni^{III}-O-N^{IV} interaction, see Supplementary Fig. S13).

ii) The in situ conductance reaches to a relatively steady second stage (1.15–1.40 V_{RHE}) with the accumulation of Co^{III}–OH* species.

iii) This is followed by the third inclining stage (1.40–1.55 V_{RHE}) corresponding to the formation of high-valence Co^{IV}–OH* (or the consequent formation of O*/OOH*, as active species that are key to OER[30,46,65]).

In addition, the evolution of oxygenated species on β-$Co(OH)_2$ are identified in ETS signals (Supplementary Fig. S14), which corresponds well with the conclusions from advanced X-ray characterizations[66], explaining the weaker OER activity compared to α-$Co(OH)_2$.

Recently, Co/Ni-based (or derived) oxyhydroxides have been widely employed as catalysts for the electro-oxidation of organic substances, which simultaneously demonstrate relatively good OER activities. To systematically study the intrinsic correlations between OER and EOOR on Co/Ni-based oxyhydroxides, we synthesized a series of bimetallic NiCo hydroxides (α-$Co_xNi_{1-x}(OH)_2$) by a co-deposition method[67]. The X-ray diffraction (XRD) patterns of as-prepared materials are shown in Supplementary Fig. S6a, which stay closely to the standard PDF cards of α-$Co(OH)_2$ (JCPDS #46-0605)[67–69] and α-$Ni(OH)_2$ (JCPDS #38-0715)[70]. The scan electron microscopy (SEM) images (Supplementary Figs. S7 and S8) indicate the morphology of the nanosheet assemblies. All α-$Co_xNi_{1-x}(OH)_2$) samples show similar electrochemical active surface areas (ECSAs) determined by CV measurements (Supplementary Figs. S18–20). The atomic ratios of Co/Ni in different hydroxide samples were determined by inductively coupled plasma optical emission spectrometer (ICP-OES) characterizations (Supplementary Tables S3 and S4), indicating the successful synthesis of target Co/Ni ratios.

We then tested the OER (@1.615 V_{RHE}) and EOOR current densities (@1.450 V_{RHE}) in a divided H-type cell for each hydroxide catalyst. These working potentials for different reactions were chosen for their optimal yield and FEs (Supplementary Fig. S24). As shown in Fig. 2d, the OER and EOOR current densities (normalized by roughness factor, defined as $ECSA_{\_catalyst}/ECSA_{\_blank\ carbon\ paper}$) each show distinctive volcano-like correlations, indicating two regions in the α-$Co_xNi_{1-x}(OH)_2$ series for better OER activity (left, $x_{Ni} \le 0.5$) and better EOOR activity (right, $x_{Ni} > 0.7$). The FDCA (2,5-furandicarboxylic acid) yield (Fig. 2d) and FE determined in potentiostatic electrolysis for HMF (5-hydroxymethylfurfural) oxidation confirm the catalytic activity trend.

Our previous work found that the addition of organic molecules in α-$Ni(OH)_2$-catalyzed EOOR would actively consume the oxygenated species ($Ni^{3+\delta}$–OH*/O*) initiated by partial-OER[11]. The typical in situ electrical transport (ETS) characteristic presented in Fig. 2c confirms the similar process on α-$Co_{0.5}Ni_{0.5}(OH)_2$. The α-$Ni(OH)_2$ starts to show a clear phase transition only after the formation of Ni^{4+}–OH* at high oxidation potentials (typically >1.40 V_{RHE}), while the α-$Co(OH)_2$ or α-$Co_{0.5}Ni_{0.5}(OH)_2$ demonstrates an additional intermediate conductive stage indicative of Co^{3+}–OH* at lower potential range (~1.00–1.20 V_{RHE}) due to the different d orbital configuration $(t_{2g})^6$ of Co^{3+} centers (and hence the double-exchange pathways) as compared to Ni. The ETS signals in this low potential region (~1.00–1.20 V_{RHE}) also show a significantly reduced value, indicating that part of Co^{2+} sites are presumably occupied by the co-adsorbed organic molecules before their oxidation, leading to a reduced surface coverage of Co^{3+}–OH*. With increasing electrochemical potentials (Fig. 2c), the ETS signals observed in EOOR show a similar inclining trend while remaining below the values in OER. This indicates that the Co^{3+}–OH* contributes to the oxidation of organic molecules under EOOR conditions, providing in situ experimental evidence to the previously suggested processes regarding oxidation ability of Co^{3+} [38].

The in situ Raman spectroscopy of α-$Co_{0.5}Ni_{0.5}(OH)_2$ and α-$Co_{0.15}Ni_{0.85}(OH)_2$ that located at two volcano plot vertexes in Fig. 2d for EOOR (Fig. 2e, f) further provides spectroscopic evidence for different co-adsorption characteristics of organics and OER-initiated oxygenated intermediates (of which the in situ Raman spectroscopy during OER can be found in Supplementary Figs. S26 and S27). As shown in Supplementary Fig. S27, the vibrational peaks of $\delta(Ni^{III}–O)$ (~480 cm^{-1}) and $\upsilon(Ni^{III}–O)$ (~550 cm^{-1}) indicating formation of oxyhydroxides[11,71] begin to be observed at 1.20 V_{RHE} for α-$Co_{0.5}Ni_{0.5}(OH)_2$ and at 1.30 V_{RHE} for α-$Co_{0.15}Ni_{0.85}(OH)_2$. The OER-relevant $\upsilon(O–O^-)$ peak (~1060 cm^{-1})[72] becomes obvious at 1.40 V_{RHE} for both catalysts. In the presence of organic molecules (Fig. 2e, f), the emergence of $\delta(Ni^{III}–O)$ and $\upsilon(Ni^{III}–O)$ peaks appear at higher electrochemical potential (1.30 V_{RHE} for α-$Co_{0.5}Ni_{0.5}(OH)_2$ and 1.35 V_{RHE} for α-$Co_{0.15}Ni_{0.85}(OH)_2$), which further supports the model of co-adsorption and surface reaction revealed by ETS. Most important, the distinct character of the $\upsilon(O–O^-)$ peak for the two catalysts demonstrates the different reaction pathways for OER and EOOR. As the higher consumption rate of Ni^{4+}–OH* species (by organic oxidation) prohibits subsequent OER steps, the $\upsilon(O–O^-)$ peak in α-$Co_{0.15}Ni_{0.85}(OH)_2$ almost disappears, while the peak in α-$Co_{0.5}Ni_{0.5}(OH)_2$ (labeled by light blue rectangle Fig. 2e remains almost unchanged. This leads to the tendency to complete the OER cycle rather than proceeding with EOOR. The schematic illustration of surface processes on the catalysts that favor OER and EOOR pathway is shown in Fig. 2g, h.

The in situ EIS measurements[41,73,74] (Supplementary Figs. S28–30) provide charge transfer resistance (R_{ct}) under different conditions. For catalysts with higher EOOR activity, a reduced R_{ct} value from OER to EOOR conditions ($R_{ct}^{EOOR} < R_{ct}^{OER}$) can be observed, consistent to the faster electro-kinetics probably from the reactions between OH* and Sub*. Opposite trend ($R_{ct}^{EOOR} > R_{ct}^{OER}$) was observed for catalysts with poor EOOR activity, suggesting the preference of O*/OOH* formation pathway.

Overall, from the catalytic activity and *operando* analysis of OER and EOOR, we qualitatively confirm the proposed EOOR mechanism and general kinetic trends derived in Fig. 1. In this case, the EOOR activity can be evaluated by the parameters correlated to the surface micro-kinetics. These key *operando* surface parameters, however, still calls for precise experimental quantification approaches.

Quantitative characterization of *operando* oxygenated species using Fourier transformed alternating current voltammetry (FTacV)

As revealed by the above analysis of the in situ surface co-adsorption and reactions, we assume that the electro-oxidation of organics on oxyhydroxides complies with a "surface electron transfer-chemical reaction (surface EC) model", where E stands for the electron transfer step from surface M^{2+}–H_2O* to $M^{3+\delta}$–OH* species (Eqs. 1 and 2), which are not accompanied with any atomic rearrangement and thus kinetically much faster compared to the following steps, and C stands for all the following surface steps with relatively slow kinetics regarding the oxidation of organic molecules (Eqs. 3–5). As both the surface electron transfer E steps and the subsequent C steps collectively contribute to the d.c. CV/LSV signals, it is difficult to precisely identify/quantify the electrochemically generated surface active $M^{3+\delta}$–OH* sites. To this end, the FTacV signaling has been demonstrated as an

https://doi.org/10.1038/s41467-024-54318-7

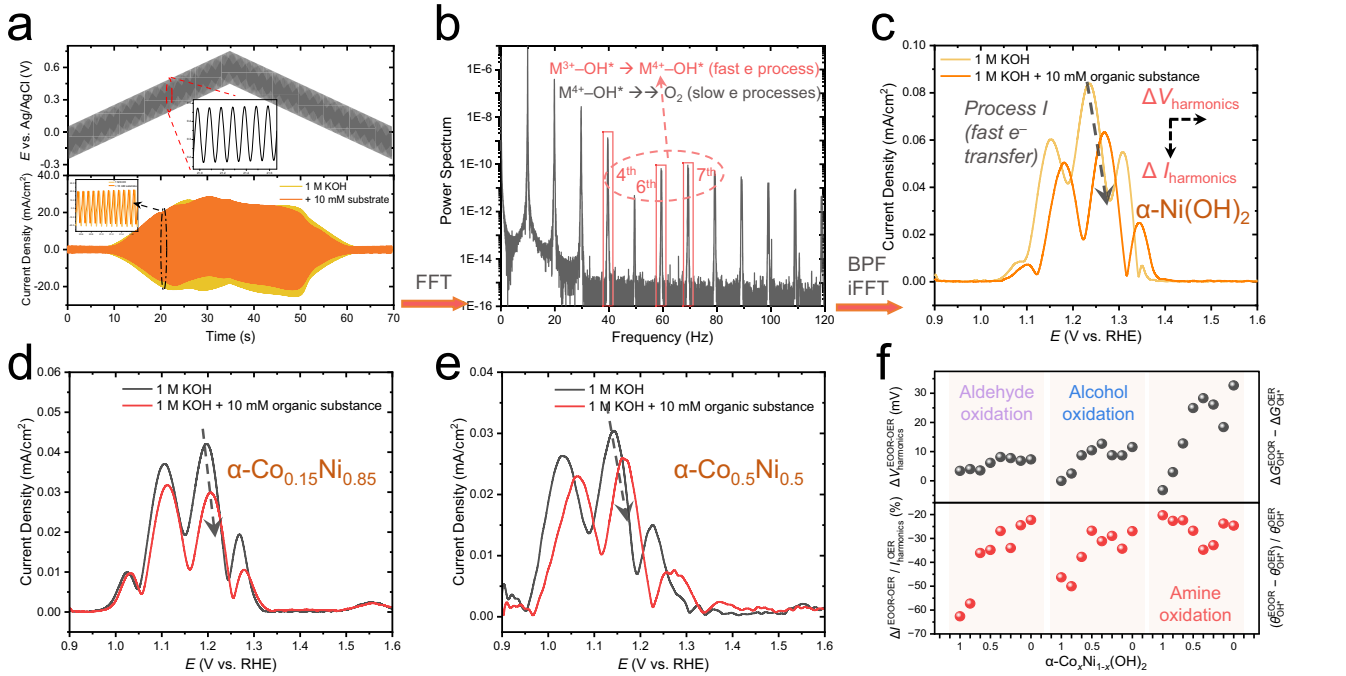

Fig. 3 | The principle and results of the FTacV measurements on OER and EOOR. **a** The applied electrochemical potential (d.c. + a.c.) and collected overall currents. **b** The power spectrum of overall current processed after fast Fourier transformation (FFT) and the target harmonics (marked by a red box and a dashed arrow) filtered by a band pass filter (BPF) followed with inverse FFT (iFFT) algorithms. **c** The $\Delta I_{harmonics}$ and $\Delta V_{harmonics}$ parameters extracted from the harmonics of α-Ni$(OH)_2$. The FTacV harmonic responses for α-$Co_{0.15}Ni_{0.85}(OH)_2$ (**d**) and α-$Co_{0.5}Ni_{0.5}(OH)_2$ (**e**) in 1.0 M KOH and the addition of 10 mM organic substances (benzylamine). Here both the absolute values of peak currents and the peak potentials (*Process I*) change, as labeled by dashed arrows, indicating the varied $\theta_{M(3+\delta)-OH^*}$ and ΔG_{OH^*}. All electrochemical data were presented without *iR*-correction. The size of carbon papers (C.P.) was 1 × 2 cm^2. **f** Summarized values of the two physio-chemical descriptors ($\Delta I^{EOOR-OER}_{harmonics}/I^{OER}_{harmonics}$ and $\Delta V^{EOOR-OER}_{harmonics}$) in the electro-oxidation of aldehyde (furfural), alcohol (furfuryl alcohol), and amie (benzylamine).

effective methodology that delicately decouples the relatively fast interfacial electron transfer from non-Faradic and complexed chemical processes[75], as demonstrated in the studies of biological redox enzymes[76–78] and heterogenous catalysis[79–83].

As illustrated in Fig. 3a, FTacV superimposes a large-amplitude sine wave on a linearly scanned electrochemical potential ramp. When there are no redox active species, the alternating current (a.c.) ideally originates only from the charge/discharge capacitance at the applied frequency f[83]. In the presence of an electrochemical redox process, the collected current includes both non-Faradaic charging and Faradaic charge transfer current. Due to the nonlinearity of the Faradaic interface (equivalent of a R_{ct}–C circuit), the overall applied potential waveform (d.c. + a.c.) can generate harmonics at f, $2f$, $3f$ … nf[84]. These nonlinear high-order harmonic components can be collected at a high sampling rate (Fig. 3a, bottom panel), and later be transformed to the power spectrum in the frequency domain by fast Fourier transformation (FFT) (see Fig. 3b). The target harmonics can be processed by a band pass filter (BPF) to filter the extra components, and finally converted to original time domain using an inverse FFT (iFFT) algorithm, as illustrated in Fig. 3c. These high-order harmonics (>4f) in the time domain are highly sensitive to the fast surface electron transfer step, with negligible contribution from subsequent, comprehensive, yet slow electron transfer and chemical processes[85]. As a result, FTacV analysis appears to be ideal for quantitative characterization of surface intermediates ($Co^{3+\delta}$/$Ni^{3+\delta}$–OH*) formed through fast electron transfer step (Eqs. 1 and 2), and for micro-electro-kinetics investigations on α-$Co_xNi_{1-x}(OH)_2$, while excluding interference from subsequent chemical steps in the surface EC model and diffusion-controlled factors in d.c. CV signals.

The proposed reactions in a water-assisted EOOR system are listed below, where Eqs. 1 and 2 represent the fast E process and the other reactions are designated as C steps.

$$M^{2+} - H_2O^* \rightleftharpoons M^{3+} - OH^* + e^- + H^* - O(\mu_2O) \quad \textit{initial OER step } (1^{st}) \tag{1}$$

$$M^{3+} - OH^* \rightleftharpoons M^{4+} - OH^* + e^- \quad \textit{initial OER step } (1.5^{th}) \tag{2}$$

$$M^{2+/3+} - ^* + \text{substance} \rightarrow M^{2+/3+} - \text{substance}^* \quad \textit{organic adsorption} \tag{3}$$

$$M^{3+/4+} - OH^* + \text{substance}^* \rightarrow\rightarrow \text{product}^* \quad \textit{catalytic oxidation} \tag{4}$$

$$\text{product}^* \rightarrow * + \text{product} \quad \textit{organic desorption} \tag{5}$$

$$M^{4+} - OH^* + OH^- \rightleftharpoons M^{4+} - O^* + H_2O + e^- \quad \textit{RDS of OER } (2^{nd}) \tag{6}$$

$$M^{4+} - O^* + OH^- \rightleftharpoons M^{4+} - OOH^* + e^- \quad \textit{late OER step } (3^{rd}) \tag{7}$$

$$M^{4+} - OOH^* + OH^- \rightleftharpoons M^{4+} - OO^* + H_2O + e^- \quad \textit{late OER step } (4^{th}) \tag{8}$$

$$M^{4+} - OO^* \rightarrow * + O_2 \quad O_2 \textit{ evolution} \tag{9}$$

The FTacV measurements were conducted systematically on α-$Co_xNi_{1-x}(OH)_2$ to investigate surface formation of $Co^{3+\delta}$/$Ni^{3+\delta}$–OH*

species and their variations from OER to EOOR, with the results shown in Fig. 3c–f. As the 5th harmonics (~50 Hz) is attenuated by the power frequency filter and worse peak shape of the 7th harmonics (Supplementary Fig. S38), the 6th harmonics were extracted and used to analysis. First, the harmonics in the OER condition can be partitioned into two parts (illustrated in Fig. 3c): *Process I* (~1.05–1.40 V_{RHE}) and *Process II* (~1.40–1.60 V_{RHE}) based on the previous studies[80,81]. *Process I* is associated with the formation of surface $Co^{3+\delta}/Ni^{3+\delta}$–OH* species, while *Process II* at higher potentials is coupled to the following steps that govern the OER (e.g., formation of $Co^{3+\delta}/Ni^{3+\delta}$–O*)[80,81]. Since the potentials for $Ni^{II\to III}$ transition (Eq. 1) and $Ni^{III\to IV}$ transition (Eq. 2) are close[30], only one set of peaks were observed in Fig. 3c. In contrast, the potential difference is more significant between $Co^{II\to III}$ and $Co^{III\to IV}$ transitions (Fig. 2b), and the two E transfer processes of Co can be clearly distinguished in *Process I* peaks (Supplementary Fig. S39). Nevertheless, in the Ni case, as the intrinsic kinetic for Eq. 2 is presumably faster than Eq. (1) judging by the comparison of complexity from both steps (see rate constants fitting results in Supplementary Table S2 according to our recent work[86]), the main peak is expected to originate from the $Ni^{III\to IV}$ transition with higher rate constant (Eq. 2).

Based on the general "surface confined catalysis"[78,79,83,85,87] model where the concentration of a surface electroactive species follows the Nernst equation with no thermodynamic (single and constant E^0) or kinetic dispersion (single and constant k^0), the quantitative parameters including the surface concentration of active sites and rate constant (of the elementary step corresponding to the fast electron transfer process) can be extracted from the simulation of FTacV data using the MECSim package[88], ($I_{harmonics} \propto c_{M^{\delta+}-OH^*}$, see more detailed discussions on the mathematical model in Supplementary Note 6). As shown in the simulation results in Supplementary Fig. S40, the peaks in the *Process I* region and the surface redox conversion in the d.c. CV correlate well with experimental results. Therefore, the partial-OER-initiated EOOR on α-$Co_xNi_{1-x}(OH)_2$ indeed fits into a surface EC mechanism, where the generation of electrochemically active $M^{3+\delta}$–OH* species (Eqs. 1 and 2) are followed by the spontaneous reaction between $M^{2+\delta}$–Sub* and $M^{3+\delta}$–OH* (Eq. 4). For quantitative analysis in this work, during the water-oxidation-assisted EOOR, the adsorption of organic substance to form $M^{2+\delta}$–Sub* will in turn occupy the available sites for the OH*, practically reduce the surface coverage of $M^{3+\delta}$–OH* (as compared to intrinsic $M^{3+\delta}$–OH* coverage during OER). As confirmed in Fig. 3c–f, with the addition of 10 mM organics, the FTacV harmonic peak current of *Process I* shows an obvious decrease in value. On this basis, we take a step forward to focus more on the change in coverage of active $M^{3+\delta}$–OH* species (designated as $\Delta\theta_{OH^*}/\theta^{OER}_{OH^*} = (\theta^{EOOR}_{OH^*} - \theta^{OER}_{OH^*})/\theta^{OER}_{OH^*}$) by calculating the relative change in harmonic peak currents:

$$\frac{I^{EOOR}_{harmonics} - I^{OER}_{harmonics}}{I^{OER}_{harmonics}} = \frac{k'(c^{EOOR}_{surface\ OH^*} - c^{OER}_{surface\ OH^*})/c_{overall\ sites}}{k'c^{OER}_{surface\ OH^*}/c_{overall\ sites}} = \frac{\theta^{EOOR}_{OH^*} - \theta^{OER}_{OH^*}}{\theta^{OER}_{OH^*}} \quad (10)$$

As a result, the FTacV harmonic peak currents quantitatively reveal the formation of surface $Co^{3+\delta}/Ni^{3+\delta}$–OH* (fast e transfer process), apart from other surface-C-contributed currents and non-Faradic signals in d.c. CV.

On the other hand, from the thermodynamic perspective, the d.c. CV peak potentials have been frequently used to estimate the free energy difference ($\Delta G_{O^*} - \Delta G_{OH^*}$) for the rate-determining step M^{3+}–OH* → $M^{3+\delta}$–O* + e^- on Ni oxyhydroxides during OER[57,89,90]. However, the d.c. CV peak positions can be easily influenced by factors such as scan rate, non-Faradaic charging current, and chemical catalytic current (see Supplementary Fig. S21 and S41), making it less efficient in the study of more complicated bi-molecular surface reactions. To this aim, high-order FTacV harmonic signals only reflect the corresponding fast-kinetic transitions (excluding solution phase reactants and structural rearrangement as in other elementary steps), thereby offering unique advantages for the potential-dependent thermodynamic evaluation of the key kinetic-fast electron transfer step[91]. Specifically, as OER and EOOR mechanism (Eqs. 1–9) share the same fast electron transfer step ($M^{\delta+}$–OH* → $M^{\delta+1}$–OH* + e^-, Eq. 2), the shifted *Process I* main peak values in harmonics ($\Delta V_{harmonics}$ from OER to EOOR in Fig. 3c–f) correlate to the changed formation free energy of $M^{\delta+1}$–OH* (ΔG_{OH^*}, as also illustrated by red ladder in Fig. 4c) under the interference of organics. Note that the observed electrochemical potentials were intrinsically determined by both equilibrium potentials of the reaction and the activation energies regarding the transitions state, quantifying exact value of ΔG_{OH^*} is still challenging. To this end, the $\Delta V_{harmonics}$ values (V) measured by FTacV is numerically equivalent to $\Delta\Delta G^{EOOR-OER}_{OH^*}$ (defined as $\Delta\Delta G^{EOOR-OER}_{OH^*} = \Delta G^{EOOR}_{OH^*} - \Delta G^{OER}_{OH^*}$), which can therefore be used to evaluate the variations in different EOORs that share the same thermodynamic parameters with OER pathway. Meanwhile, it can be confirmed that negligible potential-dependent diffusion and kinetic contributions from OH* formation itself and subsequent steps was observed in the FTacV peak potentials (and therefore $\Delta V_{harmonics}$), see experimental results and theoretical discussions in Supplementary Fig. S41 and Supplementary Note 8. This parameter ($\Delta V_{harmonics}$) is therefore of great significance towards catalyst design as it represents an intrinsic thermodynamic factor that determines whether the electrocatalytic reactions favors the EOOR or OER pathways ($\Delta\Delta G^{EOOR-OER}_{OH^*}$), which can be rationally modulated by tailoring the electronic structures of metal sites for different organic substances.

Mechanistic investigations and catalyst design principles for water-oxidation-assisted EOOR systems by two *operando* physio-chemical descriptors extracted from high-order FTacV harmonics

With the two key *operando* physio-chemical descriptors ($\Delta\theta_{OH^*}/\theta^{OER}_{OH^*}$ and $\Delta\Delta G^{EOOR-OER}_{OH^*}$) extracted from high-order FTacV harmonics, we can effectively quantify the partial-OER-assisted electro-organic oxidation processes following a surface EC model (i.e., surface electrochemical OH* generation (E) → L-H bimolecular reaction between OH* and Sub* (C) mechanism), from both electro-micro-kinetic and thermodynamic aspects. Additionally, the small Pearson coefficient (~0.22, see Supplementary Fig. S42) indicates insignificant correlation between the two physio-chemical descriptors, suggesting their distinct representations (from thermodynamic and micro-kinetic perspectives) in the mechanistic investigation on the surface electro-catalytic processes. Therefore, we expand this methodology to different electro-organic oxidation reactions with different catalytic systems, including electrocatalytic oxidation of alcohol (to either aldehyde or carboxylic acids), aldehyde (to carboxylic acids), and amine (to nitriles), to seek more detailed electro-kinetic rules that apply to the general EOORs following the electrochemical EC model, regardless of the kinetically-insignificant details on adsorption states of organic substances[92]. Other electro-catalytic organic oxidations aiming for their complete conversion to CO_2, such as Pt-catalyzed methanol oxidation for fuel cell applications reactions, may also comply with this category (with key RDS to be surface reactions between OH* and CO*/CHO*[93–96]) but are not the major focus in this investigation. Analogous to our previously-developed analytical approach[97], we draw two-dimensional catalytic activity diagrams from the two descriptors to study the relationship between surface coverage alternation of key intermediates ($\Delta\theta_{OH^*}/\theta^{OER}_{OH^*}$) and the change in ΔG_{eq2} ($\Delta\Delta G^{EOOR-OER}_{OH^*}$) with the yield of oxidation products, the results are shown in Fig. 5. For more systematic performance analysis, the catalytic performance diagrams constructed by the conversion, yield, selectivity and FE can be found in Supplementary Fig. S45. Specifically, for model EOORs that have relatively easy-to-activate substrates with few side reactions (confirmed by the HPLC/GC quantification, see Supplementary Fig. S31), the conversion is generally high, and the reaction yield is equivalent to

https://doi.org/10.1038/s41467-024-54318-7

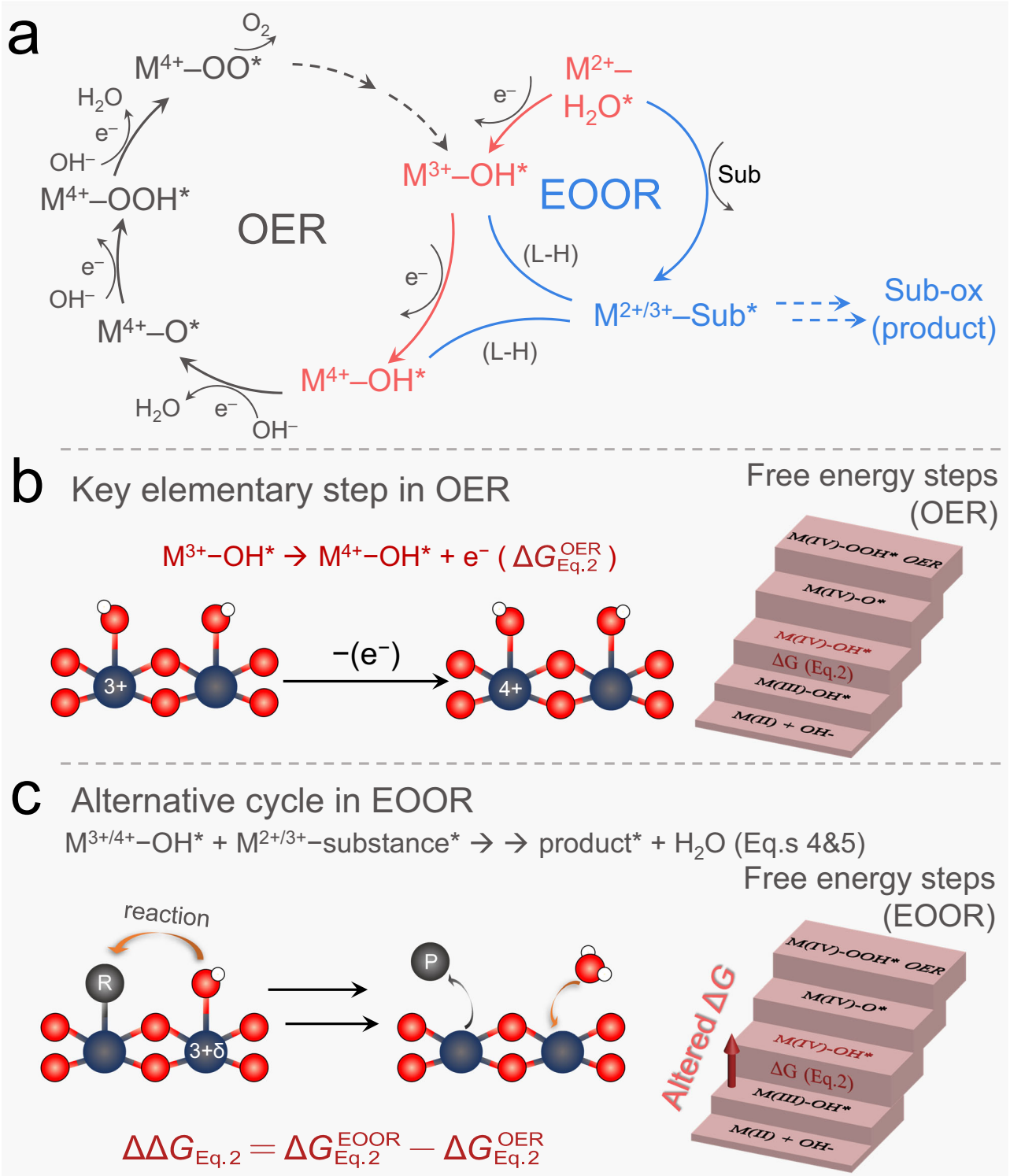

Fig. 4 | Schematic diagrams of the proposed OER and EOOR pathways and Gibbs free energy steps under two conditions. The proposed OER and EOOR pathways with shared initial steps (**a**) and schematic illustration of the electrochemical generation of $Co^{3+\delta}/Ni^{3+\delta}$–OH* species during OER and EOOR, and the Gibbs free energy steps under the two conditions. **b** The vital fast-kinetic electron transfer step (marked in red) and free energy steps during OER. **c** The vital fast-kinetic electron transfer step and altered free energy steps (marked in red arrow) during EOOR, under the influence of organics oxidation. The dark blue, red, and white balls represent the metal site, oxygen, and hydrogen atoms, respectively. "R" represents the organic substance, "P" represents the oxidation product and superscript "*" indicates the adsorbed species.

the selectivity. In the case of multiple possible products (such as alcohol to aldehyde or carboxylic acid conversion) when selectivity is critical, it can be divided into two separate reactions (alcohol to aldehyde and alcohol to carboxylic acid) for performance consideration. Furthermore, FE correlates to the overall energy efficiency in EOORs and reflects other non-organic side reactions such as OER. It is therefore a relatively independent parameter from yield/selectivity offering additional information.

https://doi.org/10.1038/s41467-024-54318-7

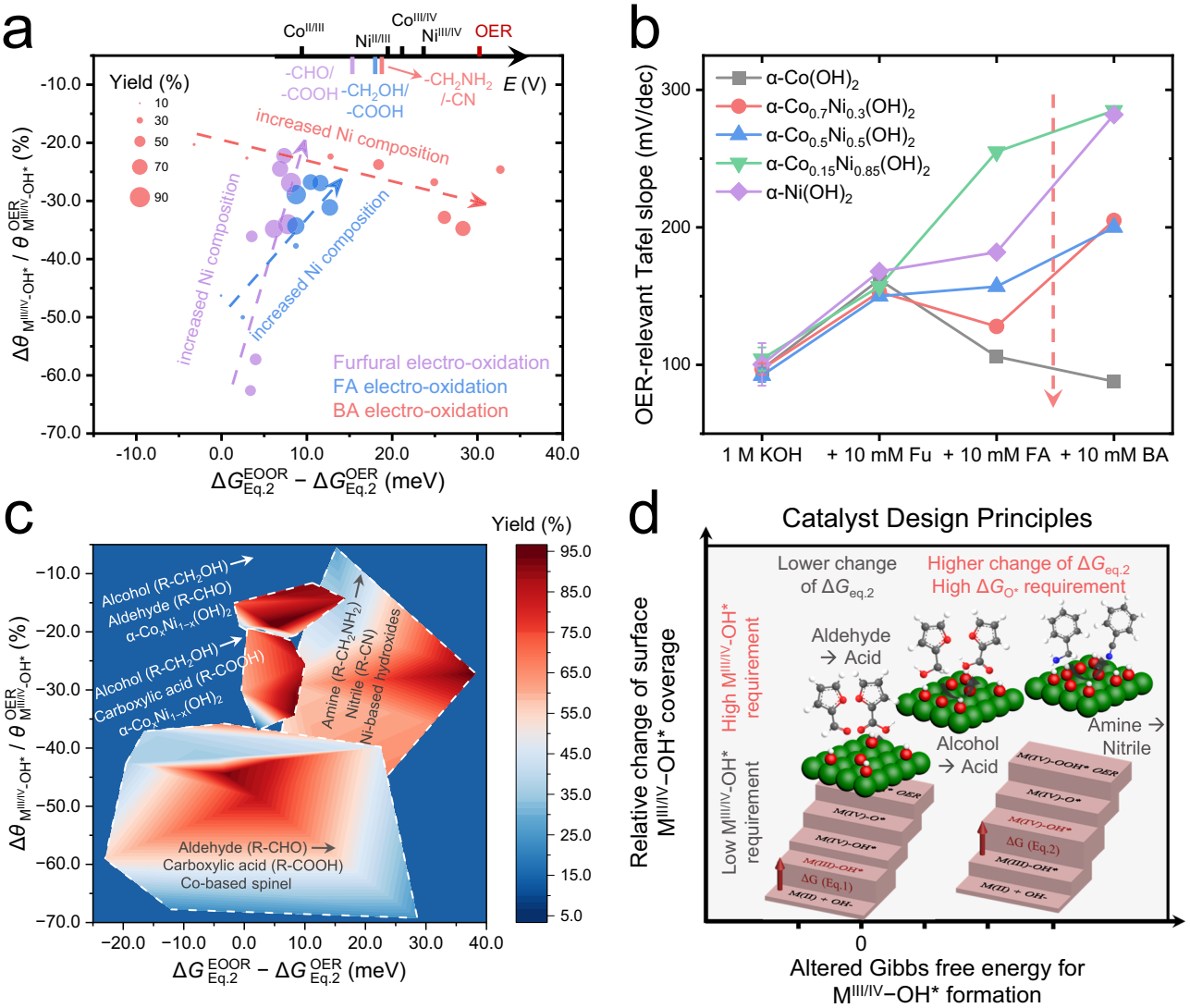

Fig. 5 | The summarized catalytic activity diagrams for EOORs, using two *operando* physio-chemical descriptors. The summarized catalytic activity diagrams for three EOORs catalyzed by α-$Co_xNi_{1-x}(OH)_2$ (**a**) and four catalyst systems (**c**). The experimentally measured oxidation potential sequence of transition mental sites and organic substances in 1 M KOH is presented in the top axis of (**a**). **b** The OER-relevant Tafel slopes derived in the kinetic Tafel region (at the potential range of 1.5–1.6 V_{RHE}, where the $FE_{OER} > 80\%$). "Fu", "FA" and, "BA" represent furfural, furfuryl alcohol and benzylamine, respectively. Error bars were obtained from three independent experiments. The dashed arrows indicate the decreased OER-relevant Tafel slopes in the case of alcohol and amine oxidation from high Ni contents to high Co contents. **d** The catalysts design principles for the efficient organics electro-oxidation. The red arrows indicate the altered free energy steps during EOOR. The green, red, white, and gray balls represent the metal site, oxygen, hydrogen atoms, and the carbon atoms in different substances, respectively.

We first study the α-$Co_xNi_{1-x}(OH)_2$ catalyzed EOOR, with furfural, furfuryl alcohol, and benzylamine as model substances to represent alcohol, aldehyde, and amine oxidations. As shown in Fig. 5a, we observe correlations between the reaction yields (illustrated by the size of circles) and the two physio-chemical parameters, indicating the distinct surface $M^{3+\delta}$–OH* coverages and the free energy variations in each catalytic system that determine the oxidation performance. For compositional analysis, the α-$Co_xNi_{1-x}(OH)_2$ catalysts exhibit a relatively high yield (~80%) for aldehyde oxidation with increasing Ni/Co ratios, which is accompanied by a significantly elevated $\Delta\theta_{OH^*}/\theta_{OH^*}^{OER}$ and negligible change in $\Delta\Delta G_{OH^*}^{EOOR-OER}$, as illustrated by the green dashed arrow in Fig. 5a. This trend in α-$Co_xNi_{1-x}(OH)_2$ indicates that Co sites favor high surface coverage of aldehyde molecule, whereas Ni sites in oxyhydroxides help maintain the original surface $Ni^{3+\delta}$–OH* coverage under adsorption competition of aldehydes, until an optimal level that effectively promotes the efficiency of surface aldehyde oxidation. As shown in Fig. 5b, each of the α-$Co_xNi_{1-x}(OH)_2$ catalysts exhibit an increased OER-relevant Tafel slope (derived from kinetic Tafel region[98] and potential range of 1.5–1.6 V_{RHE}, see Supplementary Fig. S23, where the OER electro-dynamics are dominant, i.e., $FE_{OER} > 80\%$), from an identical value of ~97 mV/dec to another identical value of ~155 mV/dec with the addition of 10 mM aldehydes. This behavior indicates that systematic uniformity exists in α-$Co_xNi_{1-x}(OH)_2$ catalyzed aldehyde electro-oxidation, probably due to the collectively altered OER RDS from Eq. 6 to the 1st step (Eq. 1) in the low-OER-overpotential region[53,99].

In comparison, the data points representing amine oxidation collectively appear more to the top and right direction of the aldehyde region in the activity diagram (see red points in Fig. 5a), demonstrating the effective oxidation of amines induces similarly optimized $\Delta\theta_{OH^*}/\theta_{OH^*}^{OER}$ (relatively higher surface $M^{3+\delta}$–OH* coverage) and significantly positive $\Delta\Delta G_{OH^*}^{EOOR-OER}$. The characteristic $\Delta\theta_{OH^*}/\theta_{OH^*}^{OER}$ indicates a relatively lower binding energy of the amine molecules to occupy the catalytic sites, which yet appears to be consistent with

different Co/Ni ratios (and therefore less determining on the catalytic performance). In sharp contrast, the more positive $\Delta\Delta G_{OH^*}^{EOOR-OER}$ indicates that the adsorption and subsequent electro-oxidation of amines greatly interfere with $M^{3+\delta}$–OH* formation on α-$Co_xNi_{1-x}(OH)_2$ ($x < 0.3$), which is closely linked to the final yield in amine oxidation. This result can be rationalized by the different complexity in the reaction pathways: while electro-oxidation of aldehydes involves only insertion of one oxygen atom, oxidation of amines requires overcoming the extra barriers of multiple oxidation/dehydrogenation steps (Eq. S70)[11,56]. The more complicated elementary steps for amine oxidation consume more active OH* species per $M^{3+\delta}$ site during a turnover cycle, leading to the stronger average interactions between $M^{3+\delta}$–OH* and adsorbed amine species, and consequently the more severe interference with OER cycle (experimentally observed more positive $\Delta\Delta G_{OH^*}^{EOOR-OER}$. The significantly increased Ni-dependent OER-relevant Tafel slopes (Fig. 5b) are also consistent with the slower OER-kinetics, resulting from the higher barriers of OER under the amine oxidation conditions. In addition, amine molecules generally have higher oxidation potentials than aldehydes and alcohols[56,100] (as depicted in top axis of Fig. 5a), which favors the catalysts with higher ΔG_{O^*} to keep a high level of $M^{3+\delta}$–OH* coverage to achieve amines oxidation at a faster reaction rate, which is also practically relevant as the nitrile products can be hydrolyzed under aqueous reaction conditions.

As for the alcohol oxidation, higher Ni ratios (≥50%) provide balanced adsorption sites and active $M^{3+\delta}$–OH* species for alcohol-to-carboxylic acids conversion, as illustrated by the blue points in Fig. 5a. The alcohol oxidation points in the α-$Co_xNi_{1-x}(OH)_2$ activity diagram located in the moderate $\Delta\theta_{OH^*}/\theta_{OH^*}^{OER}$ and $\Delta\Delta G_{OH^*}^{EOOR-OER}$ regions, closer to the aldehydes' oxidation region (red points), presumably due to the similar yet slightly more complex oxidation mechanisms (dehydrogenation and subsequent insertion of one O atom, see equation S71), which is consistent with the previous conclusion that aldehydes and alcohols dominantly undergo "indirect oxidation" and "potential-dependent oxidation", respectively[43,92]. In addition, note that the $Co^{3+\delta}$–OH* species has closed oxidation potentials with alcohols and amines, and thus incapable of oxidizing the two molecules (negligible oxidation yield from low-Ni-catalysts, see Fig. 5a). Therefore, the competitive OER cycle proceeds more easily on the Co sites, and its OER-relevant Tafel slopes decrease in the case of alcohol and amine oxidation from high Ni contents to high Co contents (illustrated by dashed arrow in Fig. 5b).

For molecules that are more challenging to be activated (with less polarity), such as toluene and cyclohexene (model substrates for selective oxidation of benzyl C-H bonds and selective epoxidation of alkenes, respectively), the corresponding FTacV results were shown in Supplementary Fig. S43. The minimal variation in signals indicates weak organic adsorptions even under high anodic potentials, which are consistent with their chemical inertness. In such cases, in situ generating extra strongly oxidizing radicals (such as Cl· or Br·)[86,101] or redox mediators (such as HOCl)[102] is presumably required to achieve high yields. Based on the innovation and scalability of measurement and kinetics analysis methods, key information and conclusions that were not easily obtained in previous literature have been obtained in this work.

In sum, from the spatial distribution of the descriptor points, the adsorption and subsequent oxidation of three organics on the surface of α-$Co_xNi_{1-x}(OH)_2$ catalysts would cause different levels of interference toward the OER cycles. Specifically:

- the more negative $\Delta\theta_{OH^*}/\theta_{OH^*}^{OER}$ indicates the larger (lower) surface coverage of organics (oxygenated species),
- the more positive $\Delta\Delta G_{OH^*}^{EOOR-OER}$ demonstrates the increased free energy barrier of $M^{3+\delta}$–OH* formation due to additional interactions between surface organic intermediates and OH* species and insufficient active $M^{3+\delta}$–OH* species for OER.

This two-descriptor system thus provides a convenient, efficient, and systematic evaluation of the catalytic mechanisms and preferred kinetic conditions at the microscopic level.

With the successful application of two key FTacV-derived physio-chemical descriptors that lead to the construction of catalytic activity diagram for α-$Co_xNi_{1-x}(OH)_2$-catalyzed alcohol, aldehyde, and amine electro-oxidations, we aim to further extend this analytical strategy to other electro-oxidation reactions that share a similar water-oxidation-assisted (surface EC) oxidation mechanism. To this end, we chose spinel (Co-based) catalyzed Fu oxidation[50], α-$Co_xNi_{1-x}(OH)_2$ catalyzed benzyl alcohol selective oxidation to benzaldehyde and benzoic acid (Supplementary Fig. S34), and Ni-based hydroxide catalyzed benzylamine oxidation[11] as model systems to represent the four EOORs with more suitable catalyst categories. After the FTacV high-order harmonics data acquisition and processing, we constructed a general catalytic activity diagram for these EOORs, as shown in Fig. 5c. Interestingly, with the varying catalyst materials spreading across a wider range in both descriptors, we can more clearly observe separated reaction "hot-zones" for the four reactions. Note that the 2D activity diagram derived from d.c. CV (see Supplementary Figs. S46 and S47) appears ineffective for the same task, because the position of redox peaks is easily influenced by the scan rate, non-Faradaic, and chemical catalytic currents. Specifically, the catalysts for aldehyde oxidation in Fig. 5c are Co-based oxyhydroxides (amorphous, derived from electrochemical reconstruction of spinel sulfides)[50], which demonstrate close values of $\Delta\Delta G_{OH^*}^{EOOR-OER}$ with α-$Co_xNi_{1-x}(OH)_2$ in Fig. 5a, yet more negative $\Delta\theta_{OH^*}/\theta_{OH^*}^{OER}$, since more oxygen vacancies on amorphous Co oxyhydroxides are more beneficial for organic adsorption over Co^{3+}–OH*. The near-zero and even negative $\Delta\Delta G_{OH^*}^{EOOR-OER}$ also indicates a possible change of the OER RDS from Eq. 6 to the 1st step (Eq. 1) under aldehyde oxidation on Co-based oxyhydroxides[53,99] (arrows in free energy steps in Fig. 5d), which is consistent with the speculation drawn by OER-Tafel analysis in Fig. 5b. The characteristic trend and high-yield regions of benzyl alcohol (to benzoic acid) and benzylamine oxidations are close to that in Fig. 5a, where the Mn-doped α-$Ni(OH)_2$ demonstrates better activity for amine oxidation[11] because Mn doping greatly increases the ΔG_{O^*} of α-$Ni(OH)_2$ to further hamper the OER pathway and increase $M^{3+\delta}$–OH* coverage. The selective electro-oxidation of benzyl alcohol to benzaldehyde can be efficiently achieved by reducing pH and water activity (with more cations)[103] to decrease the θ_{OH^*}. The summarized parameters for the four types of EOORs are listed in Table 1.

It is worth mentioning that the $\Delta(\Delta G_{OH^*})$ values we measured under different EOOR conditions (Table 1), caused by the competitive adsorption and consumption of active OH* by organic molecules, correlate well to the variation in OH* adsorption energy during OER simulated by changing the number of active sites in the literature (less than 25-50 meV)[53]. It further reveals the power of FTacV measurement as an effective tool to experimentally obtain key physio-chemical parameters that have only been provided by the parameter fitting in theoretical micro-kinetic simulation/analysis. The parameter of $\Delta\Delta G_{OH^*}^{EOOR-OER}$ thus effectively indicates the *operando* interactions between the two surface species (closely correlated to the micro-kinetic complexity of substance oxidation processes). Combining with $\Delta\theta_{OH^*}/\theta_{OER}$ that represents the decreased *operando* surface coverage of OH* species, these two physio-chemical descriptors enable visualization of the electro-kinetic and thermodynamic aspects of the reaction system from a microscopic level. Therefore, the two key descriptors provide effective catalysts design principles for organics electro-oxidation via the modulation of surface coverages and Gibbs free energy of $M^{3+\delta}$–OH* (Fig. 5d). For the consideration of traditional kinetic analysis, experimental quantification of these *operando* physio-chemical

Table 1 | Summarized key parameters and design principles for EOOR systems

Substances	Products	Oxidation Potential	Relative Change of θ_{OH^*} [a]	Reaction Complexity	Altered $\Delta G_{Eq.2}$	$M^{3+\delta}$–OH* Requirement
Aldehyde	Carboxylic acid	Low	25–55%	Simple	−5 to 5 meV	Relatively low level of θ_{OH^*}
Alcohol	Aldehyde	Highest [b]	13–20%	Simple	0–12 meV [b]	Relatively low level of θ_{OH^*}
	Carboxylic acid	Moderate	25–35%	Moderate	5–10 meV	Balanced $\theta_{OH^*}/\theta_{sub^*}$
Amine	Nitrile	High	20–32%	Complex	20–35 meV	High level of θ_{OH^*}

[a]Coverage relative to the θ_{OH^*} under OER conditions.
[b]In weak alkaline solution (1 M K_2CO_3).

descriptors provides the precise numbers of key parameters such as optimal surface $\theta_{sub^*}/\theta_{OH^*}$ (in Fig. 1a, b), which is otherwise difficult to obtain[104], thus providing effective guidance for catalysts improvement. It is also relevant to note that effective performance prediction maps were developed using apparent electrochemical parameters for homogenous electro-organic synthesis[97] and photo-generated electrochemical charge for homogenous photo-organic synthesis[105], respectively, offering improved efficiency and robustness for constructing machine learning (ML) models compared with DFT-descriptors[106]. However, construction of the reactivity diagram from d.c. CV-derived parameters is inefficient for the heterogeneous electro-catalytic organic oxidations targeted in this study. As classical electrochemical organic synthesis on inert electrodes such as glassy carbon typically does not involve surface adsorption/micro-reactions[107,108] (i.e., the organic substance presumably undergoes an interfacial electron transfer process with a simple collision on the electrodes and proceeds with homogeneous reactions), more intrinsic physio-chemical parameters are necessary to achieve precise and efficient representation of the (surface) chemical space for machine learning (ML) investigations in heterogeneous electrocatalysis.

In summary, by using in situ electrical transport, Raman characterization, and FTacV measurements, we systematically studied three EOORs catalyzed by the Co/Ni oxyhydroxides (classic OER catalysts), in which both surface adsorbed organic molecules and active $M^{3+\delta}$–OH* species (their surface coverages, interactions and etc.) are critical to determine the micro-electrokinetics of the reaction. We developed here two key *operando* physio-chemical descriptors ($\Delta\theta_{OH^*}/\theta_{OH^*}^{OER}$ and $\Delta\Delta G_{OH^*}^{EOOR-OER}$) to quantitatively determine the generation and consumption of active intermediates, which further leads to construction of an electro-catalytic activity diagram exhibiting characteristic regions for the different organic oxidations, effective for active sites recognition, mechanistic evaluation, and catalyst modulation. General design principles can be summarized for the future catalyst development with improved electro-oxidation efficiency:

i. Aldehyde oxidation typically requires no harsh conditions, the catalysts should provide enough sites through vacancies creation, metal leaching, or amorphization for molecular adsorption and $M^{3+\delta}$–OH* generation, which can be typically achieved by amorphous Co oxyhydroxides.
ii. The efficient oxidation of amines benefits from catalysts with higher energy barriers of ΔG_{O^*} to keep a high level of surface active $Ni^{3+\delta}$–OH* for fast catalytic reaction.
iii. The good catalysts for alcohol oxidation typically own a moderate energy barrier of ΔG_{OH^*} and balanced $\theta_{sub^*}/\theta_{OH^*}$.
iv. The efficiently selective oxidation of alcohol to aldehyde could be achieved by reducing the surface θ_{sub^*} and θ_{OH^*} via lowering pH and/or water activity.

The methodology established in this work not only unravels the in-depth microscopic details during electro-oxidation processes but also provides an efficient fast-screening method to discover and design high-performance heterogeneous electrocatalysts.

Methods

Synthesis of bimetallic NiCo hydroxides (α-$Co_xNi_{1-x}(OH)_2$)

A series of α-$Co_xNi_{1-x}(OH)_2$ with varying Ni content was synthesized via a co-deposition method[67]. In a typical procedure, x mmol ($0 < x < 1$) of $Co(NO_3)_2{\cdot}6H_2O$ and 0.20 g of polyvinylpyrrolidone were dissolved in 40 mL of distilled water, forming a clear pink solution after sonication. This solution was then transferred to a three-necked flask and stirred with an electric agitator at 1000 rpm. Next, 40 mL of freshly prepared $NaBH_4$ (0.12 g) solution was slowly added with continuous vigorous stirring, turning the mixture black. Immediately afterward, 40 mL of $NiCl_2{\cdot}6H_2O$ ($1-x$ mmol) solution was introduced dropwise into the black mixture. After all reagents were added, the reaction was maintained under stirring for 6 h at room temperature (25 °C). The final product was collected by centrifugation, washed three times with ethanol and distilled water, and dried in an oven at 60 °C for 6 h.

Synthesis of α-$Co(OH)_2$

Single-component α-$Co(OH)_2$ was prepared similarly with the procedure of α-$Co_xNi_{1-x}(OH)_2$ but without the addition of $NiCl_2{\cdot}6H_2O$ solution.

Synthesis of α-$Ni(OH)_2$

The pure α-$Ni(OH)_2$ was prepared using a solvothermal approach, following a previously reported method[70]. Briefly, 1 mmol of $Ni(NO_3)_2{\cdot}6H_2O$ was dissolved in 20 mL of ethanol, followed by the quick addition of 2 mL oleylamine and 10 mL ethanol. This mixture was stirred for 30 min to achieve homogeneity, then transferred to a 50 mL Teflon-lined autoclave. The autoclave was sealed and heated to 180 °C for 15 h in a convection oven, then allowed to cool naturally to room temperature. The resulting green precipitate was collected, washed several times with cyclohexane, ethanol, and distilled water, and dried under vacuum at 60 °C for 6 h.

Synthesis of β-$Co(OH)_2$

The β-$Co(OH)_2$ was prepared following a modified hydrothermal method. Typically, 1 mmol $Co(NO_3)_2{\cdot}6H_2O$ was dissolved into 20 mL 18.2 MΩ·cm H_2O, then a mixture of oleylamine (2 mL) and ethanol (10 mL) was quickly added. The mixture was stirred for 0.5 h, which was then transferred into a 50 mL Teflon-lined autoclave. The autoclave was sealed and maintained at 180 °C for 15 h and then cooled naturally to room temperature. The resulting pink precipitant was collected and washed with cyclohexane, ethanol, and distilled water several times and was then dried under vacuum at 60 °C for 6 h.

Materials characterization

The as-synthesized samples were examined by XRD, which was carried out on a Shimadzu Lab X/XRD-6000 X-ray diffractometer equipped with a Cu-Kα radiation source ($\lambda = 1.5418$ Å) operating at 40 kV and 30 mA. SEM images were recorded on Hitachi S-4800 with samples deposited on carbon conductive tapes. Inductively coupled plasma optical emission spectrometer (ICP-OES) (PerkinElmer Avio500) was used to test the Co/Ni ratios of the series of as prepared and post-electrolysis catalysts.

Electrochemical measurements

Typically, 5 mg of catalyst was dispersed in ethanol (480 μL), ultrapure water (18.2 MΩ·cm, 480 μL) and Nafion solution (5 wt% in ethanol, 40 μL) to form a well-dispersed ink. For fabrication of the working electrode, 50 μL of the catalyst ink was dropped onto 1 × 2 cm^2 carbon paper. The electrode was then dried at room temperature. The mass loading of the catalyst was 0.25 mg·cm^{-2}. All electrochemical measurements were carried out at 23–25 °C in this work.

Electrochemical experiments were performed in a typical three-electrode system using a CS3004 multichannel potentiostat (CorrTest Instruments). All electrochemical cell components were cleaned with ultra-pure H_2O (18.2 MΩ·cm) prior to experiments. All potentials were referenced to an Ag/AgCl reference electrode (in 3.5 M KCl), and platinum wire was used as the counter electrode in all measurements. The measured potential vs. $E_{Ag/AgCl}$ was converted to reverse hydrogen electrode potential (RHE) based on the Nernst equation, $E_{RHE} = E_{vs.\ Ag/AgCl} + 0.059 \times pH + 0.2046$ V, which was further calibrated by CV curves in 1.0 M KOH (99.999%) (Supplementary Fig. S10). The CV tests were carried out after pumping high-purity hydrogen for 30 min to saturate the electrolyte. All electrochemical data were presented without *iR*-correction. All the catalysts were tested after the electrochemical pre-activation (50 cycles of d.c. CV with the range of 0.9 ~1.45 V vs. RHE) to achieve a steady surface state.

Electrolysis experiments

10 mg catalyst was dispersed in 1 mL ethanol with ultrasonic dispersion for 30 min and the 40 μL Nafion solution (5 wt%) was added into the homogeneous suspension with ultrasonic dispersion for another 20 min. Then a certain amount of homogeneous suspensions were dropped onto the carbon paper (C.P., 1 × 2 cm^2). Ultimately, the anode electrode with a mass loading of 2.0 mg/cm^2 was prepared and was employed in the electrolysis measurement.

All electrolysis measurements were performed in a typical three-electrode system using a CS3004 electrochemical workstation in 1.0 M KOH. Hg/HgO (1.0 M KOH) and Pt electrodes were used as reference electrode and counter electrode, respectively. The potentials were quoted with respect to the RHE through $E_{RHE} = E_{Hg/HgO} + 0.059 \times pH + 0.098$ V. The separators of H-cell were anion exchange membranes (AEM). All electrochemical data were presented without *iR*-correction. The electro-oxidation of organic substrates was similar to OER, except that the electrolyte was performed in 1.0 M KOH solution with the addition of 10 mM furfural, furfuryl alcohol, benzyl alcohol, HMF or benzylamine. The potentials for Faradaic efficiency and selectivity measurements were 1.40 V_{RHE} for HMF, furfural and furfuryl alcohol, 1.46 V_{RHE} for benzylamine, 1.42 V_{RHE} for benzyl alcohol to benzoic acid, 1.54 V_{RHE} for benzyl alcohol to benzaldehyde (in 1 M K_2CO_3).

In situ Raman spectroscopy measurements

In situ Raman spectroscopy test was performed using HORIBA XploRA PLUS Raman microscope with the laser wavelength of 532 nm. The Raman spectroscopy were captured (50 s × 2) with laser intensity filtered to 1%. The electrochemical potential was applied by a potentiostat (CHI 660E).

Fourie transformed alternating current voltammetry (FTacV) measurements

An arbitrary waveform generator (Keysight 33250A) was used to generate a sine wave to superposition on the direct current (d.c.) CV electrochemical potential exported by a custom-built potentiostat (CS150H, CorrTest Instruments). All the catalysts were tested after the electrochemical pre-activation (50 cycles of d.c. CV with the range of 0.9–1.45 V vs. RHE) to achieve a steady surface state. The a.c. voltametric experiments were undertaken with an amplitude of $\Delta E = 160$ mV, which provides an adequate level of nonlinearity to allow higher order harmonics to be detected, and at the same time, does not induce very significant ohmic losses and broadening[61,79–81,83,84,109]. The frequency of $f = 9.876$ Hz provides a sufficient level of kinetic sensitivity[81,84]. For better Faraday-sensitive signal detection and noise rejection, the mass loading of the catalyst was reduced to 0.10 mg·cm^{-2} in FTacV tests. All electrochemical data were presented without *iR*-correction. Scan rate of ac CV measurements was set as 20 mV·s^{-1}, sampling rate was fixed at 1000 Sa·s^{-1} in this work. Fast Fourier transform (FFT) codes were adopted to convert the time domain raw data into the frequency domain power spectrum. Then a series of harmonics were BPF and then converted to corresponding time domain data via iFFT codes.

Data availability

The authors declare that the data supporting the conclusions of this study are available within the paper and its supplementary materials. Source data of figures are provided in this paper. Additional data are available from the corresponding author upon request.

References

1. Oener, S. Z., Foster, M. J. & Boettcher, S. W. Accelerating water dissociation in bipolar membranes and for electrocatalysis. *Science* **369**, 1099–1103 (2020).
2. Suen, N.-T. et al. Electrocatalysis for the oxygen evolution reaction: recent development and future perspectives. *Chem. Soc. Rev.* **46**, 337–365 (2017).
3. Hong, W. T. et al. Toward the rational design of non-precious transition metal oxides for oxygen electrocatalysis. *Energy Environ. Sci.* **8**, 1404–1427 (2015).
4. Bajdich, M., García-Mota, M., Vojvodic, A., Nørskov, J. K. & Bell, A. T. Theoretical investigation of the activity of cobalt oxides for the electrochemical oxidation of water. *J. Am. Chem. Soc.* **135**, 13521–13530 (2013).
5. Sun, Y. et al. Highly selective electrocatalytic oxidation of benzyl C–H using water as safe and sustainable oxygen source. *Green Chem.* **22**, 7543–7551 (2020).
6. Lum, Y. et al. Tuning OH binding energy enables selective electrochemical oxidation of ethylene to ethylene glycol. *Nat. Catal.* **3**, 14–22 (2020).
7. Wang, T. et al. Combined anodic and cathodic hydrogen production from aldehyde oxidation and hydrogen evolution reaction. *Nat. Catal.* **5**, 66–73 (2022).
8. Chen, W. et al. Activity origins and design principles of nickel-based catalysts for nucleophile electrooxidation. *Chem* **6**, 2974–2993 (2020).
9. Huang, Y., Chong, X., Liu, C., Liang, Y. & Zhang, B. Boosting hydrogen production by anodic oxidation of primary amines over a NiSe nanorod electrode. *Angew. Chem. Int. Ed.* **57**, 13163–13166 (2018).
10. Lin, R. et al. Identification and manipulation of dynamic active site deficiency-induced competing reactions in electrocatalytic oxidation processes. *Energy Environ. Sci.* **15**, 2386–2396 (2022).
11. Sun, Y. et al. Highly selective electrocatalytic oxidation of amines to nitriles assisted by water oxidation on metal-doped α-$Ni(OH)_2$. *J. Am. Chem. Soc.* **144**, 15185–15192 (2022).
12. Bender, M. T., Yuan, X. & Choi, K.-S. Alcohol oxidation as alternative anode reactions paired with (photo)electrochemical fuel production reactions. *Nat. Commun.* **11**, 4594 (2020).
13. Zhou, H., Li, Z., Ma, L. & Duan, H. Electrocatalytic oxidative upgrading of biomass platform chemicals: from the aspect of reaction mechanism. *Chem. Commun.* **58**, 897–907 (2022).
14. Huang, C., Huang, Y., Liu, C., Yu, Y. & Zhang, B. Integrating hydrogen production with aqueous selective semi-

dehydrogenation of tetrahydroisoquinolines over a Ni_2P bifunctional electrode. *Angew. Chem. Int. Ed.* **58**, 12014–12017 (2019).
15. Li, T. et al. Photoelectrochemical oxidation of organic substrates in organic media. *Nat. Commun.* **8**, 390 (2017).
16. Trotochaud, L., Young, S. L., Ranney, J. K. & Boettcher, S. W. Nickel–iron oxyhydroxide oxygen-evolution electrocatalysts: the role of intentional and incidental iron incorporation. *J. Am. Chem. Soc.* **136**, 6744–6753 (2014).
17. Burke, M. S., Kast, M. G., Trotochaud, L., Smith, A. M. & Boettcher, S. W. Cobalt–Iron (Oxy)hydroxide oxygen evolution electrocatalysts: the role of structure and composition on activity, stability, and mechanism. *J. Am. Chem. Soc.* **137**, 3638–3648 (2015).
18. Dionigi, F. et al. In-situ structure and catalytic mechanism of NiFe and CoFe layered double hydroxides during oxygen evolution. *Nat. Commun.* **11**, 2522 (2020).
19. Yu, M., Budiyanto, E. & Tüysüz, H. Principles of water electrolysis and recent progress in cobalt-, nickel-, and iron-based oxides for the oxygen evolution reaction. *Angew. Chem. Int. Ed.* **61**, e202103824 (2022).
20. Zhou, D. et al. NiFe hydroxide lattice tensile strain: enhancement of adsorption of oxygenated intermediates for efficient water oxidation catalysis. *Angew. Chem. Int. Ed.* **58**, 736–740 (2019).
21. Bai, L., Hsu, C.-S., Alexander, D. T. L., Chen, H. M. & Hu, X. Double-atom catalysts as a molecular platform for heterogeneous oxygen evolution electrocatalysis. *Nat. Energy* **6**, 1054–1066 (2021).
22. Zhang, Z. et al. Selectively anchoring single atoms on specific sites of supports for improved oxygen evolution. *Nat. Commun.* **13**, 2473 (2022).
23. You, H. et al. Monolayer niir-layered double hydroxide as a long-lived efficient oxygen evolution catalyst for seawater splitting. *J. Am. Chem. Soc.* **144**, 9254–9263 (2022).
24. Yang, H. et al. Intramolecular hydroxyl nucleophilic attack pathway by a polymeric water oxidation catalyst with single cobalt sites. *Nat. Catal.* **5**, 414–429 (2022).
25. Wang, C. et al. Engineering lattice oxygen activation of iridium clusters stabilized on amorphous bimetal borides array for oxygen evolution reaction. *Angew. Chem. Int. Ed.* **60**, 27126–27134 (2021).
26. Kang, J. et al. Valence oscillation and dynamic active sites in monolayer NiCo hydroxides for water oxidation. *Nat. Catal.* **4**, 1050–1058 (2021).
27. Pei, Z. et al. Highly efficient electrocatalytic oxygen evolution over atomically dispersed synergistic Ni/Co dual sites. *Angew. Chem. Int. Ed.* **61**, e202207537 (2022).
28. Zhai, P. et al. Engineering single-atomic ruthenium catalytic sites on defective nickel-iron layered double hydroxide for overall water splitting. *Nat. Commun.* **12**, 4587 (2021).
29. Garcia, A. C., Touzalin, T., Nieuwland, C., Perini, N. & Koper, M. T. M. Enhancement of oxygen evolution activity of nickel oxyhydroxide by electrolyte alkali cations. *Angew. Chem. Int. Ed.* **58**, 12999–13003 (2019).
30. Tian, B. et al. Double-exchange-induced in situ conductivity in nickel-based oxyhydroxides: an effective descriptor for electrocatalytic oxygen evolution. *Angew. Chem. Int. Ed.* **60**, 16448–16456 (2021).
31. Zheng, X. et al. Origin of enhanced water oxidation activity in an iridium single atom anchored on NiFe oxyhydroxide catalyst. *Proc. Natl. Acad. Sci. USA* **118**, e2101817118 (2021).
32. Wu, T. et al. Spin pinning effect to reconstructed oxyhydroxide layer on ferromagnetic oxides for enhanced water oxidation. *Nat. Commun.* **12**, 3634 (2021).
33. Duan, Y. et al. Anodic oxidation enabled cation leaching for promoting surface reconstruction in water oxidation. *Angew. Chem. Int. Ed.* **60**, 7418–7425 (2021).
34. Hao, Y. et al. Electrode/electrolyte synergy for concerted promotion of electron and proton transfers toward efficient neutral water oxidation. *Angew. Chem. Int. Ed.* **62**, e202303200 (2023).
35. Govind Rajan, A., Martirez, J. M. P. & Carter, E. A. Facet-independent oxygen evolution activity of pure β-NiOOH: different chemistries leading to similar overpotentials. *J. Am. Chem. Soc.* **142**, 3600–3612 (2020).
36. Kanan, M. W. et al. Structure and valency of a cobalt–phosphate water oxidation catalyst determined by in situ X-ray spectroscopy. *J. Am. Chem. Soc.* **132**, 13692–13701 (2010).
37. Li, N. et al. Influence of iron doping on tetravalent nickel content in catalytic oxygen evolving films. *Proc. Natl. Acad. Sci. USA.* **114**, 1486–1491 (2017).
38. Deng, X. et al. Understanding the roles of electrogenerated Co^{3+} and Co^{4+} in selectivity-tuned 5-hydroxymethylfurfural oxidation. *Angew. Chem. Int. Ed.* **60**, 20535–20542 (2021).
39. Ge, R. et al. Selective electrooxidation of biomass-derived alcohols to aldehydes in a neutral medium: promoted water dissociation over a nickel-oxide-supported ruthenium single-atom catalyst. *Angew. Chem. Int. Ed.* **61**, e202200211 (2022).
40. Lu, Y. et al. Integrated catalytic sites for highly efficient electrochemical oxidation of the aldehyde and hydroxyl groups in 5-hydroxymethylfurfural. *ACS Catal.* **12**, 4242–4251 (2022).
41. Qi, Y. et al. Insights into the activity of nickel boride/nickel heterostructures for efficient methanol electrooxidation. *Nat. Commun.* **13**, 4602 (2022).
42. Tao, H. B. et al. A general method to probe oxygen evolution intermediates at operating conditions. *Joule* **3**, 1498–1509 (2019).
43. Bender, M. T., Lam, Y. C., Hammes-Schiffer, S. & Choi, K.-S. Unraveling two pathways for electrochemical alcohol and aldehyde oxidation on NiOOH. *J. Am. Chem. Soc.* **142**, 21538–21547 (2020).
44. Yang, G. et al. Unraveling the mechanism for paired electrocatalysis of organics with water as a feedstock. *Nat. Commun.* **13**, 3125 (2022).
45. Chung, M. et al. Direct propylene epoxidation via water activation over Pd-Pt electrocatalysts. *Science* **383**, 49–55 (2024).
46. Shin, H., Xiao, H. & Goddard, W. A. III In silico discovery of new dopants for Fe-doped Ni oxyhydroxide ($Ni_{1-x}Fe_xOOH$) catalysts for oxygen evolution reaction. *J. Am. Chem. Soc.* **140**, 6745–6748 (2018).
47. Liu, H. et al. Vitamin C-assisted synthesized Mn–Co oxides with improved oxygen vacancy concentration: boosting lattice oxygen activity for the air-oxidation of 5-(Hydroxymethyl)furfural. *ACS Catal.* **11**, 7828–7844 (2021).
48. Woo, J. et al. Collaborative electrochemical oxidation of the alcohol and aldehyde groups of 5-hydroxymethylfurfural by NiOOH and $Cu(OH)_2$ for superior 2,5-furandicarboxylic acid production. *ACS Catal.* **12**, 4078–4091 (2022).
49. Li, R., Xiang, K., Peng, Z., Zou, Y. & Wang, S. Recent advances on electrolysis for simultaneous generation of valuable chemicals at both anode and cathode. *Adv. Energy Mater.* **11**, 2102292 (2021).
50. Wang, F. et al. Spinel-derived formation and amorphization of bimetallic oxyhydroxides for efficient electrocatalytic biomass oxidation. *J. Phys. Chem. Lett.* **14**, 2674–2683 (2023).
51. Chen, D. et al. Highly efficient biomass upgrading by a Ni-Cu electrocatalyst featuring passivation of water oxidation activity. *Angew. Chem. Int. Ed.* **62**, e202309478 (2023).
52. Schreier, M., Yoon, Y., Jackson, M. N. & Surendranath, Y. Competition between H and CO for active sites governs copper-mediated electrosynthesis of hydrocarbon fuels. *Angew. Chem. Int. Ed.* **57**, 10221–10225 (2018).
53. Zhang, J. et al. Advances in thermodynamic-kinetic model for analyzing the oxygen evolution reaction. *ACS Catal.* **10**, 8597–8610 (2020).

54. Geppert, J. et al. Microkinetic analysis of the oxygen evolution performance at different stages of iridium oxide degradation. *J. Am. Chem. Soc.* **144**, 13205–13217 (2022).
55. Zhu, X., Huang, J. & Eikerling, M. pH effects in a model electrocatalytic reaction disentangled. *JACS Au* **3**, 1052–1064 (2023).
56. Hao, Y. et al. Origin of the universal potential-dependent organic oxidation on nickel oxyhydroxide. *ACS Catal.* **13**, 2916–2927 (2023).
57. Rao, R. R. et al. Spectroelectrochemical analysis of the water oxidation mechanism on doped nickel oxides. *J. Am. Chem. Soc.* **144**, 7622–7633 (2022).
58. Ding, M. et al. An on-chip electrical transport spectroscopy approach for in situ monitoring electrochemical interfaces. *Nat. Commun.* **6**, 1–9 (2015).
59. Ding, M. et al. On-chip in situ monitoring of competitive interfacial anionic chemisorption as a descriptor for oxygen reduction kinetics. *ACS Cent. Sci.* **4**, 590–599 (2018).
60. Mu, Z. et al. On-chip electrical transport investigation of metal nanoparticles: characteristic acidic and alkaline adsorptions revealed on Pt and Au surface. *J. Phys. Chem. Lett.* **11**, 5798–5806 (2020).
61. Bond, A. M. et al. An integrated instrumental and theoretical approach to quantitative electrode kinetic studies based on large amplitude Fourier transformed a.c. voltammetry: a mini review. *Electrochem. Commun.* **57**, 78–83 (2015).
62. Gracia, J. Spin dependent interactions catalyse the oxygen electrochemistry. *Phys. Chem. Chem. Phys.* **19**, 20451–20456 (2017).
63. Gracia, J., Sharpe, R. & Munarriz, J. Principles determining the activity of magnetic oxides for electron transfer reactions. *J. Catal.* **361**, 331–338 (2018).
64. Zhang, N., Wang, C., Chen, J. & Chai, Y. Oxygen reactivity regulation via double-exchange interaction for enhanced water oxidation. *EcoMat* **5**, e12290 (2023).
65. Xiao, H., Shin, H. & Goddard, W. A. III Synergy between Fe and Ni in the optimal performance of (Ni, Fe)OOH catalysts for the oxygen evolution reaction. *Proc. Natl. Acad. Sci. USA* **115**, 5872 (2018).
66. Mefford, J. T. et al. Correlative operando microscopy of oxygen evolution electrocatalysts. *Nature* **593**, 67–73 (2021).
67. Song, J.-M. et al. A facile synthesis of graphene-like cobalt–nickel double hydroxide nanocomposites at room temperature and their excellent catalytic and adsorption properties. *J. Nanopart. Res.* **16**, 2269 (2014).
68. Xu, H. et al. Heterogeneous $Co(OH)_2$ nanoplates/Co_3O_4 nanocubes enriched with oxygen vacancies enable efficient oxygen evolution reaction electrocatalysis. *Nanoscale* **10**, 18468–18472 (2018).
69. Bao, J. et al. A ternary cobalt–molybdenum–vanadium layered double hydroxide nanosheet array as an efficient bifunctional electrocatalyst for overall water splitting. *Chem. Commun.* **55**, 3521–3524 (2019).
70. Gao, M. et al. Efficient water oxidation using nanostructured α-nickel-hydroxide as an electrocatalyst. *J. Am. Chem. Soc.* **136**, 7077–7084 (2014).
71. Hou, S. et al. Dual in situ laser techniques underpin the role of cations in impacting electrocatalysts. *Angew. Chem. Int. Ed.* **61**, e202201610 (2022).
72. Moysiadou, A., Lee, S., Hsu, C.-S., Chen, H. M. & Hu, X. Mechanism of oxygen evolution catalyzed by cobalt oxyhydroxide: cobalt superoxide species as a key intermediate and dioxygen release as a rate-determining step. *J. Am. Chem. Soc.* **142**, 11901–11914 (2020).
73. Li, S. et al. Coordination environment tuning of nickel sites by oxyanions to optimize methanol electro-oxidation activity. *Nat. Commun.* **13**, 2916 (2022).
74. Wang, H.-Y. et al. In operando identification of geometrical-site-dependent water oxidation activity of spinel Co_3O_4. *J. Am. Chem. Soc.* **138**, 36–39 (2016).
75. Zhang, J. & Bond, A. M. Theoretical studies of large amplitude alternating current voltammetry for a reversible surface-confined electron transfer process coupled to a pseudo first-order electrocatalytic process. *J. Electroanal. Chem.* **600**, 23–34 (2007).
76. Adamson, H., Bond, A. M. & Parkin, A. Probing biological redox chemistry with large amplitude Fourier- transformed ac voltammetry. *Chem. Commun.* **53**, 9519–9533 (2017).
77. Tao, L. et al. Probing electron transfer in the manganese-oxide-forming MnxEFG protein complex using fourier transformed AC voltammetry: understanding the oxidative priming effect. *ChemElectroChem* **5**, 872–876 (2018).
78. Adamson, H. et al. Electrochemical evidence that pyranopterin redox chemistry controls the catalysis of YedY, a mononuclear Mo enzyme. *Proc. Natl. Acad. Sci. USA* **112**, 14506–14511 (2015).
79. Zhang, Y. et al. Direct detection of electron transfer reactions underpinning the tin-catalyzed electrochemical reduction of CO_2 using Fourier-transformed ac voltammetry. *ACS Catal.* **7**, 4846–4853 (2017).
80. Chen, J. et al. Interfacial interaction between FeOOH and Ni–Fe LDH to modulate the local electronic structure for enhanced OER electrocatalysis. *ACS Catal.* **8**, 11342–11351 (2018).
81. Bonke, S. A., Bond, A. M., Spiccia, L. & Simonov, A. N. Parameterization of water electrooxidation catalyzed by metal oxides using Fourier transformed alternating current voltammetry. *J. Am. Chem. Soc.* **138**, 16095–16104 (2016).
82. Lertanantawong, B. et al. Study of the underlying electrochemistry of polycrystalline gold electrodes in aqueous solution and electrocatalysis by large amplitude fourier transformed alternating current voltammetry. *Langmuir* **24**, 2856–2868 (2008).
83. Snitkoff-Sol, R. Z. et al. Quantifying the electrochemical active site density of precious metal-free catalysts in situ in fuel cells. *Nat. Catal.* **5**, 163–170 (2022).
84. Hu, Z. et al. Onset of nonlinear electroosmotic flow under an AC electric field. *Anal. Chem.* **94**, 17913–17921 (2022).
85. Guo, S.-X., Bond, A. M. & Zhang, J. Fourier transformed large amplitude alternating current voltammetry: principles and applications. *Rev. Polarogr.* **61**, 21–32 (2015).
86. Ran, P. et al. Universal high-efficiency electrocatalytic olefin epoxidation via a surface-confined radical promotion. *Nat. Commun.* **15**, 8877 (2024).
87. Guo, S.-X. et al. Facile electrochemical co-deposition of a graphene–cobalt nanocomposite for highly efficient water oxidation in alkaline media: direct detection of underlying electron transfer reactions under catalytic turnover conditions. *Phys. Chem. Chem. Phys.* **16**, 19035–19045 (2014).
88. Kennedy, G. F., Bond, A. M. & Simonov, A. N. Modelling ac voltammetry with MECSim: facilitating simulation–experiment comparisons. *Curr. Opin. Electroche.* **1**, 140–147 (2017).
89. Kuznetsov, D. A. et al. Tuning redox transitions via inductive effect in metal oxides and complexes, and implications in oxygen electrocatalysis. *Joule* **2**, 225–244 (2018).
90. Zhang, J., Yang, H. B., Zhou, D. & Liu, B. Adsorption energy in oxygen electrocatalysis. *Chem. Rev.* **122**, 17028–17072 (2022).
91. Zouraris, D. & Karantonis, A. Determination of kinetic and thermodynamic parameters from large amplitude Fourier transform ac voltammetry of immobilized electroactive species. *J. Electroanal. Chem.* **876**, 114729 (2020).
92. Bender, M. T., Warburton, R. E., Hammes-Schiffer, S. & Choi, K.-S. Understanding hydrogen atom and hydride transfer processes during electrochemical alcohol and aldehyde oxidation. *ACS Catal.* **11**, 15110–15124 (2021).

93. Poerwoprajitno, A. R. et al. A single-Pt-atom-on-Ru-nanoparticle electrocatalyst for CO-resilient methanol oxidation. *Nat. Catal.* **5**, 231–237 (2022).
94. Wang, J. et al. Toward electrocatalytic methanol oxidation reaction: longstanding debates and emerging catalysts. *Adv. Mater.* **35**, 2211099 (2023).
95. Tritsaris, G. A. & Rossmeisl, J. Methanol oxidation on model elemental and bimetallic transition metal surfaces. *J. Phys. Chem. C* **116**, 11980–11986 (2012).
96. Farias, M. J. S., Cheuquepán, W., Tanaka, A. A. & Feliu, J. M. Identity of the most and least active sites for activation of the pathways for CO_2 formation from the electro-oxidation of methanol and ethanol on platinum. *ACS Catal.* **10**, 543–555 (2020).
97. Chen, Y. et al. Electro-descriptors for the performance prediction of electro-organic synthesis. *Angew. Chem. Int. Ed.* **60**, 4199–4207 (2021).
98. Van Der Heijden, O., Park, S., Eggebeen, J. J. J. & Koper, M. T. M. Non-kinetic effects convolute activity and tafel analysis for the alkaline oxygen evolution reaction on NiFeOOH electrocatalysts. *Angew. Chem. Int. Ed.* **62**, e202216477 (2023).
99. Limaye, A. M., Zeng, J. S., Willard, A. P. & Manthiram, K. Bayesian data analysis reveals no preference for cardinal Tafel slopes in CO_2 reduction electrocatalysis. *Nat. Commun.* **12**, 703 (2021).
100. Shen, K. et al. Electrochemical oxidation of methane to methanol on electrodeposited transition metal oxides. *J. Am. Chem. Soc.* **145**, 6927–6943 (2023).
101. Gao, Y. et al. Membrane-free electrosynthesis of epichlorohydrins mediated by bromine radicals over nanotips. *J. Am. Chem. Soc.* **146**, 714–722 (2024).
102. Li, Y. et al. Redox-mediated electrosynthesis of ethylene oxide from CO_2 and water. *Nat. Catal.* **5**, 185–192 (2022).
103. Xu, L. et al. Salting-out aldehyde from the electrooxidation of alcohols with 100% selectivity. *Angew. Chem. Int. Ed.* **61**, e202210123 (2022).
104. Herzog, A. et al. Operando raman spectroscopy uncovers hydroxide and CO species enhance ethanol selectivity during pulsed CO_2 electroreduction. *Nat. Commun.* **15**, 3986 (2024).
105. Dai, L. et al. Harnessing electro-descriptors for mechanistic and machine learning analysis of photocatalytic organic reactions. *J. Am. Chem. Soc.* **146**, 19019–19029 (2024).
106. Hou, X., Li, S., Frey, J., Hong, X. & Ackermann, L. Machine learning-guided yield optimization for palladaelectro-catalyzed annulation reaction. *Chem* **10**, 2283–2294 (2024).
107. Yan, M., Kawamata, Y. & Baran, P. S. Synthetic organic electrochemical methods since 2000: on the verge of a renaissance. *Chem. Rev.* **117**, 13230–13319 (2017).
108. Leech, M. C. & Lam, K. A practical guide to electrosynthesis. *Nat. Rev. Chem.* **6**, 275–286 (2022).
109. Bond, A. M., Duffy, N. W., Guo, S.-X., Zhang, J. & Elton, D. Changing the look of voltammetry. *Anal. Chem.* **77**, 186 A–195 A (2005).

Acknowledgements

B.T., F.W., P.R., L.D., Y.L., Yu.S., Z.M., Ya.S., L.T., and M.D. acknowledge the support by the Natural Science Foundation of China (22172075 and 92156024), the Fundamental Research Funds for the Central Universities in China (14380273), the Natural Science Foundation of Jiangsu Province (BK20220765) and Beijing National Laboratory for Molecular Sciences (BNLMS202107). W.A.G. acknowledges support from the U.S. Department of Energy, Office of Science, Office of Basic Energy Sciences, Fuels from Sunlight Hub under Award Number DE-SC0021266.

Author contributions

M.D. and W.A.G. supervised the research. B.T. and M.D. designed the research. B.T. conducted the various in situ measurements (ETS, Raman, FTacV, and EIS). F.W. conducted the potentiostatic electrolysis and products HPLC, GC quantification. P.R., Y.L., Yu.S., Ya.S., and L.T. participated in catalysts synthesis and characterization. B.T., L.D., P.R. and Z.M. performed the micro-kinetics simulation. B.T. and M.D. analyzed the data. B.T., F.W., W.A.G., and M.D. co-wrote the paper. All authors have given approval to the final version of the manuscript.

Competing interests

The authors declare no competing interests.

Additional information

Supplementary information The online version contains supplementary material available at https://doi.org/10.1038/s41467-024-54318-7.

Correspondence and requests for materials should be addressed to Mengning Ding.

Peer review information *Nature Communications* thanks Hui Luo who co-reviewed with Hanzhi Ye and the other, anonymous, reviewers for their contribution to the peer review of this work. A peer review file is available.